Chapter 3: Lanthanide Doping in $CsPbBr_3$ Nanocrystals: Extending the Emission in the Blue Region

3.1 Introduction

In Chapter 1, properties of pristine $CsPbX_3$ (X=Cl, Br, I) as well as lanthanide-doped $CsPbX_3$ has been discussed in detail. The stability issue is one of the major concerns of $CsPbX_3$.Various strategies has been used to increase the stability of halide perovskites like surface passivation, post synthesis treatments, doping with transition metals and lanthanide ion, etc. Lanthanide ion doping into $CsPbX_3$ improves the stability as well as impart additional properties of itself into the host, like adding one or more emission channels. Since lanthanide ions emit a range of wavelengths under particular excitations, the lanthanide-doped materials show great application in color LEDs, high-definition displays, NIR cameras, etc.

Lanthanides doping in traditional semiconductors presents challenges due to their tetrahedral structure, which provides a low coordination number of four for the central lanthanides ion [126]. In contrast, perovskite semiconductors adopt an octahedral structure, where lanthanide ions are centrally positioned within the octahedra, resulting in a higher coordination number of six. Europium (Eu) typically exhibits a stable oxidation state of +3, though the +2 state is also observed under certain conditions. The Eu^{3+}-ion emits characteristic yellow, red, and near-infrared (NIR) light due to partially allowed f-f transitions, which, however, have a low quantum yield [127][128]. Additionally, the f-f transitions of Eu^{3+} are minimally affected by the surrounding environment, making Eu^{3+} less ideal as an activator in quantum-confined inorganic halide perovskite (IHP) nanostructures. Conversely, the Eu^{2+}-ion is a highly efficient luminescent center, emitting blue light due to

its f-d transition. This transition is allowed by parity selection rules and is sensitive to the local crystal field, with the luminescence band position varying based on the Eu^{2+}-ion's local environment within the host lattice. Consequently, exploring the properties of Eu^{2+} in the quantum-confined structure of $CsPbBr_3$ for multifunctional applications is of significant interest. Due to its strong blue emission, Eu^{2+}-ions have been incorporated into various hosts for advanced applications, including scintillators, display panels, fluorescent lamps, and blue LEDs [129][130]. Several studies have examined the properties of Eu^{2+}-doped phosphors synthesized through various methods, such as solid-state reaction [131], hydrothermal [132], combustion [133], and melt quenching [134]. However, the optical properties of Eu^{2+} in IHPs remain underexplored.

In this Chapter, we investigate the structural and optical behavior of $CsPbBr_3$ and Eu^{2+}-doped $CsPbBr_3$ halide perovskite nanocrystals synthesized using the hot-injection method. Extensive structural and optical characterizations were conducted and analyzed. We observed that the emission behavior of blue and green emissions is significantly influenced by varying excitation wavelengths. The photoluminescence (PL) spectra of Eu^{2+}-doped $CsPbBr_3$ nanocrystals were examined under multi-wavelength stimuli, and detailed decay dynamics were also performed and analyzed.

3.2 Synthesis of $CsPbBr_3$ and Eu-doped $CsPbBr_3$ Nanocrystals

The $CsPbBr_3$ and Eu-doped $CsPbBr_3$ nanocrystals (NCs) are synthesized via the established hot-injection method [59], which involves a two-step process. Initially, a cesium-oleate precursor solution is prepared. In the subsequent step, this cesium-oleate solution is rapidly injected into a lead-containing solution, leading to the formation of the final product. A schematic representation of this synthesis method is provided in Fig. 2.1 of Chapter 2.

3.2.1 Synthesis of $CsPbBr_3$ NCs

Step 1: Synthesis of Cesium-Oleate Stock Solution: In a three-neck round-bottom flask, 30 mL of 1-Octadecene (ODE, Alfa Aesar) and 2.5 mL of oleic acid (OA) were added to 0.82 g of Cs_2CO_3 (99.99%, Alfa Aesar). The mixture was subjected to drying at 120°C for 30 minutes under constant argon gas flow while being continuously stirred. The temperature was then increased to 140°C, and the mixture was heated until the Cs_2CO_3 was fully dissolved, resulting in the formation of a cesium-oleate solution. This solution was reserved as a stock solution for subsequent use.

Step 2: Synthesis of $CsPbBr_3$ NCs: For the synthesis of $CsPbBr_3$ NCs, 0.5 mmol of $PbBr_2$ (99.99%, Alfa Aesar), 15 mL of ODE, 1 mL of OA (90%, Alfa Aesar), and 1 mL of oleylamine (OAm, Cis-1-amino-9-octadecene, Sigma-Aldrich) were added to a three-neck round-bottom flask. The precursor mixture was heated on a hot plate with magnetic stirring and dried at 120°C under argon gas purging for 30 minutes. The temperature was then raised to 150°C, continuing the stirring until the $PbBr_2$ was completely dissolved. At this point, 1.5 mL of the pre-heated (120°C) cesium-oleate solution was swiftly injected into the flask using a syringe. After 30 seconds, the reaction was quenched by cooling the solution to room temperature in an ice bath. The resulting solution was centrifuged at 9000 rpm for 10 minutes. The supernatant was discarded, and the obtained particles were dispersed in n-hexane for further characterization.

3.2.2 Synthesis of Eu-doped $CsPbBr_3$ NCs

To synthesize Eu-doped $CsPbBr_3$ NCs, Eu_2O_3 was used as the source of Eu^{2+}-ions. A quantity of 0.25 mmol of Eu_2O_3 (99.99%, Alfa Aesar) was dissolved in an appropriate

amount of HBr (47%, Spectrochem) to yield 0.5 mmol of $EuBr_3$. The $EuBr_3$ was then dissolved in 5 mL of ODE at 140 ºC. Separately, 0.5 mmol of $PbBr_2$ (99.99%, Alfa Aesar) was placed in a three-neck round-bottom flask, and 10 mL of ODE was added. Subsequently, 1 mL of OA and 1 mL of OAm were injected into the flask containing the $EuBr_3$ and $PbBr_2$ solution under an Ar-gas atmosphere, and the mixture was heated to 120 ºC for 1 hour. The temperature was then elevated to 180 ºC to achieve a completely dissolved solution. At this point, 1.5 mL of cesium-oleate, preheated to 120 ºC, was rapidly injected into the flask using a syringe. After 30 seconds, the flask was promptly transferred to an ice-water bath to cool the solution to room temperature and halt the reaction. The resulting solution was centrifuged at 9000 rpm for 10 minutes, and the supernatant was discarded. The collected particles were then dispersed in n-hexane for further characterization and analysis.

3.3 Results and discussion

3.3.1 Crystal structure and morphology analysis

The X-ray diffraction (XRD) analysis was conducted to examine the crystal structure and phase composition using a Miniflex 600 diffractometer from Rigaku, Japan. The measurements were performed with a step size of 0.02° over the 2θ range from 10° to 90°, utilizing Cu-Kα radiation. The XRD patterns for undoped $CsPbBr_3$ and Eu-doped $CsPbBr_3$ samples are displayed in Fig. 3.1(a) and 3.1(b), respectively. The XRD pattern of the undoped $CsPbBr_3$ matches well with the inorganic crystal standard database (ICSD) number ICSD 97-851 and aligns closely with the reported orthorhombic phase of CsPbBr3, corresponding to space group *P*bnm (62) [135]. Similar diffraction patterns have also been reported by other groups [136][137][138], confirming the orthorhombic phase of $CsPbBr_3$ perovskite. In the XRD pattern of the Eu-doped CsPbBr3 sample, the diffraction peaks

appear broader compared to the undoped $CsPbBr_3$. This broadening is noticeable for the peaks associated with the (hkl) values (020), (121), (040), (301), (240), (242), (161), (440), and (442) in Fig. 3.1(b). In contrast, these peaks are relatively sharp in the XRD pattern of the undoped $CsPbBr_3$ NCs. The broader peaks in the Eu-doped $CsPbBr_3$ NCs indicate smaller particle sizes compared to the undoped $CsPbBr_3$, as observed in Fig. 3(a) and 3(b). Despite the introduction of Eu^{2+}-ion, which have an ionic radius (1.17 Å) comparable to that of Pb^{2+}-ion (1.19 Å), no significant peak shifts were observed in the XRD pattern, indicating minimal lattice distortion due to Eu-doping.

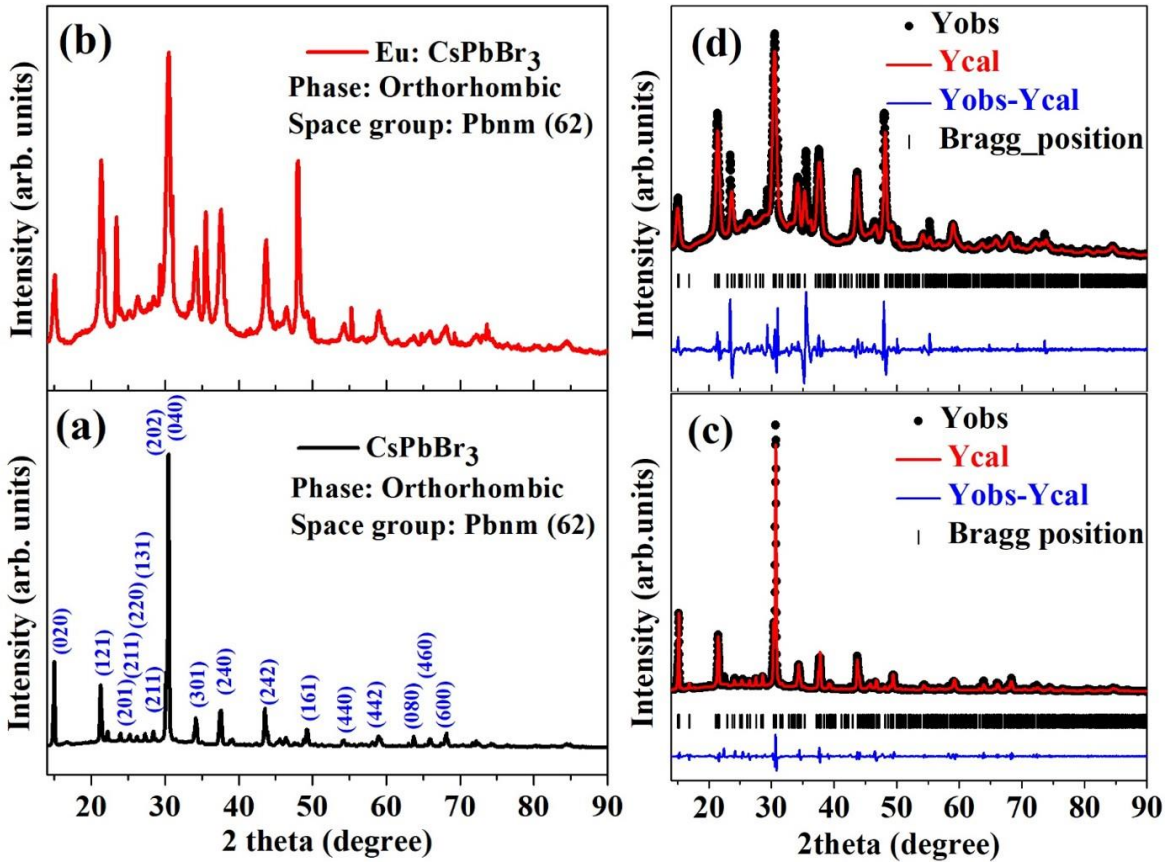

Figure 3.1: XRD patterns of (a) $CsPbBr_3$, (b) Eu-doped $CsPbBr_3$. Plots of the XRD patterns with Le-Bail refinement of the (c) $CsPbBr_3$, (d) Eu-doped $CsPbBr_3$.

To confirm the phase and space group of the synthesized samples, LeBail fitting was conducted using the "FullProf Suite" software. The results are illustrated in Fig. 3.1(c) and 3.1(d) for undoped $CsPbBr_3$ and Eu-doped $CsPbBr_3$, respectively. The Pseudo-Voigt function was chosen to accurately model the peak shapes, and the background was handled through "linear interpolation between a set of background points with refinable heights" for baseline correction. LeBail fitting for both samples ($CsPbBr_3$ and Eu-doped $CsPbBr_3$) was performed using "profile matching with a constant scale factor". The lattice parameters obtained for $CsPbBr_3$ were a = 8.23388 $\pm$ 0.00040 Å, b = 11.66364 $\pm$ 0.00028 Å, c = 8.43526 $\pm$ 0.00066 Å, with $\alpha = \beta = \gamma$ = 90°. For Eu-doped CsPbBr3, the lattice parameters were a = 8.22078 $\pm$ 0.00286 Å, b = 11.67790 $\pm$ 0.00402 Å, c = 8.46488 $\pm$ 0.00310 Å, with $\alpha = \beta = \gamma$ = 90°. Due to the nearly identical ionic radii of Pb^{2+} and Eu^{2+}-ions, the lattice parameters of undoped and Eu-doped $CsPbBr_3$ remain very similar after the partial substitution of Pb^{2+} by Eu^{2+}. The obtained results from the LeBail fitting are presented in Table 3.1.

Table 3.1 The lattice parameters of $CsPbBr_3$ and Eu: $CsPbBr_3$ sample obtained by LeBail analysis.

Parameter	**$CsPbBr_3$**	**Eu-doped $CsPbBr_3$**
Peak shape function	Pseudo-Voigt	Pseudo-Voigt
Phase	Orthorhombic	Orthorhombic
Space group	*P*bnm (62)	*P*bnm (62)
a (Å)	8.23388 $\pm$ 0.00040	8.22078 $\pm$ 0.00286
b (Å)	11.66364 $\pm$ 0.00028	11.67790 $\pm$ 0.00402
c (Å)	8.43526 $\pm$ 0.00066	8.46488 $\pm$ 0.00310
$\alpha = \beta = \gamma$ (°)	90	90
Volume ($Å^3$))	810.112 $\pm$ 0.077	812.641$\pm$ 0.496
Profile residual (*R*p)	7.31	5.85
Weighted profile residual (*R*wp)	10.90	10.4
Expected profile residual (*R*exp)	3.67	1.73

The crystal structure of pristine $CsPbBr_3$ is depicted in Fig. 3.2(a). In this structure, Br^- ions are corner-sharing with a central Pb atom, forming a $PbBr_6^{4-}$ octahedron. Fig. 3.2(b) illustrates the octahedral geometry in two distinct orientations, where the Pb atom is surrounded by six nearest-neighbor Br atoms. The Pb-Br bond lengths in this configuration are found to be 2.942(17) Å, 3.005(17) Å, and 2.967(4) Å. The calculated polyhedral volume of the $PbBr_6^{4-}$ unit is 34.8871 $Å^3$.

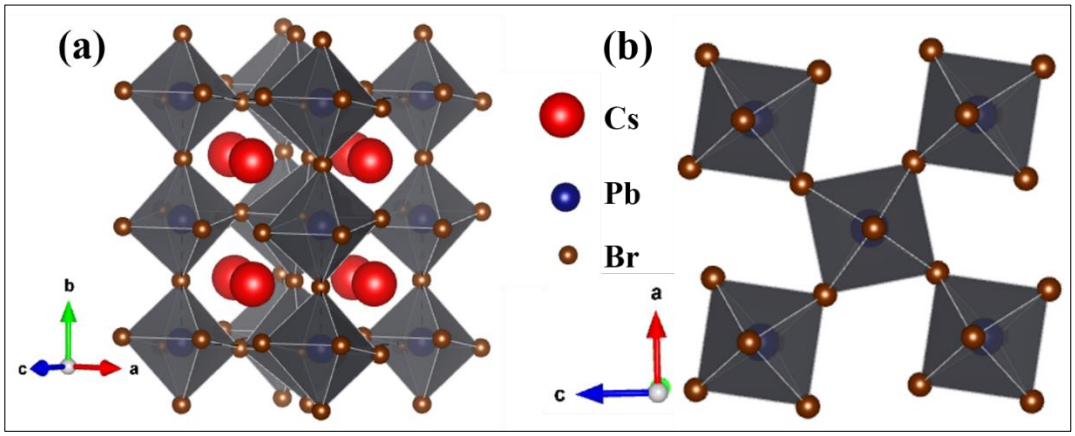

Figure 3.2: (a) Crystal structure of the $CsPbBr_3$ in orthorhombic geometry. (b) $PbBr_6^{4-}$ octahedra of $CsPbBr_3$.

High-resolution transmission electron microscopy (HR-TEM) was performed using a Tecnai G2 20 TWIN 200 kV (FEI) instrument to determine the particle size and morphology. The HR-TEM images of the synthesized $CsPbBr_3$ and Eu-doped $CsPbBr_3$ NCs are shown in Fig. 3.3(a) and 3.3(b), respectively. The synthesized $CsPbBr_3$ exhibits a non-uniform particle size distribution ranging from 12 nm to 28 nm. A histogram representing this particle size distribution is provided in Fig. 3.3(c). The particles predominantly display a cubic morphology, although some exhibit deviations, appearing non-cubic but with a tendency towards cubic structure formation. The average particle size obtained is approximately 19 nm, distribution is shown in Fig. 3.3(c). In contrast, the Eu-doped $CsPbBr_3$ NCs exhibit a

nearly uniform particle morphology, with sizes ranging between 5 nm and 10 nm. The histogram depicting the particle size distribution is presented in Fig. 3.3(d). These NCs possess a cubical morphology, with an average particle size of around 7 nm. Bigger particle size of $CsPbBr_3$ can be attributed to the uncontrolled rapid nucleation and growth during quenching. The incorporation of Eu into $CsPbBr_3$ lowers the surface energy [139], while simultaneously increasing the lattice energy of the NCs. This dual effect significantly hinders the growth rate of the NCs, resulting in a particle size of Eu into $CsPbBr_3$ that is approximately three times smaller than that of undoped $CsPbBr_3$. A similar trend of notable particle size reduction in $CsPbBr_3$ NCs upon Sb-doping was reported by Subramaniam et al. [139].

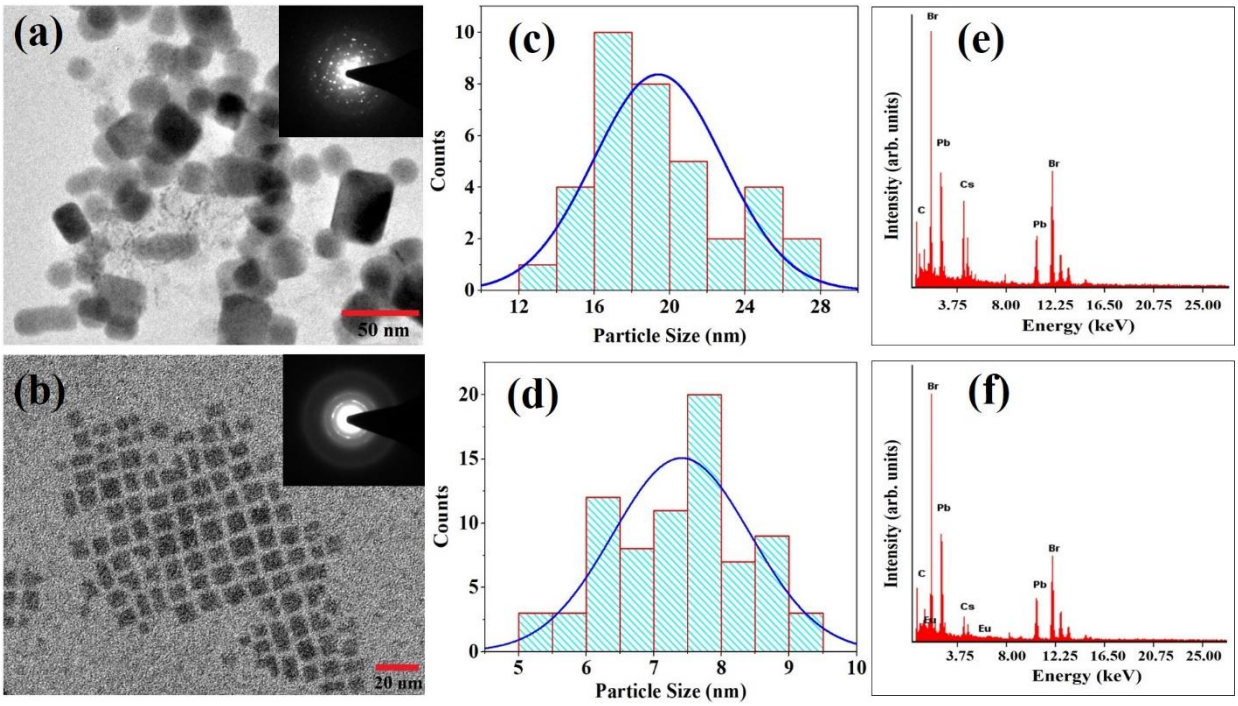

Figure 3.3: HR-TEM images of (a) $CsPbBr_3$, (b) Eu-doped $CsPbBr_3$. Histogram of the particle size distribution of synthesized (c) $CsPbBr_3$, (d) Eu-doped $CsPbBr_3$. The EDAX patterns of (e) $CsPbBr_3$, and (f) Eu-doped $CsPbBr_3$.

Energy-dispersive X-ray (EDAX) analysis has been performed for both samples, and the corresponding spectra are illustrated in Fig. 3.3(e) and 3.3(f) for $CsPbBr_3$ and Eu-doped $CsPbBr_3$, respectively. The EDAX spectra display peaks corresponding to each precursor element, thereby confirming the presence of all constituent elements in the samples.

3.3.2 UV-visible absorption spectroscopy

The UV-visible absorption spectra of the samples, measured using a JASCO V770 spectrophotometer, are depicted in Fig. 3.4. Fig. 3.4(a) illustrates the UV-visible absorption spectrum of $CsPbBr_3$ NCs, while Fig. 3.4(b) presents that of Eu-doped $CsPbBr_3$ NCs.

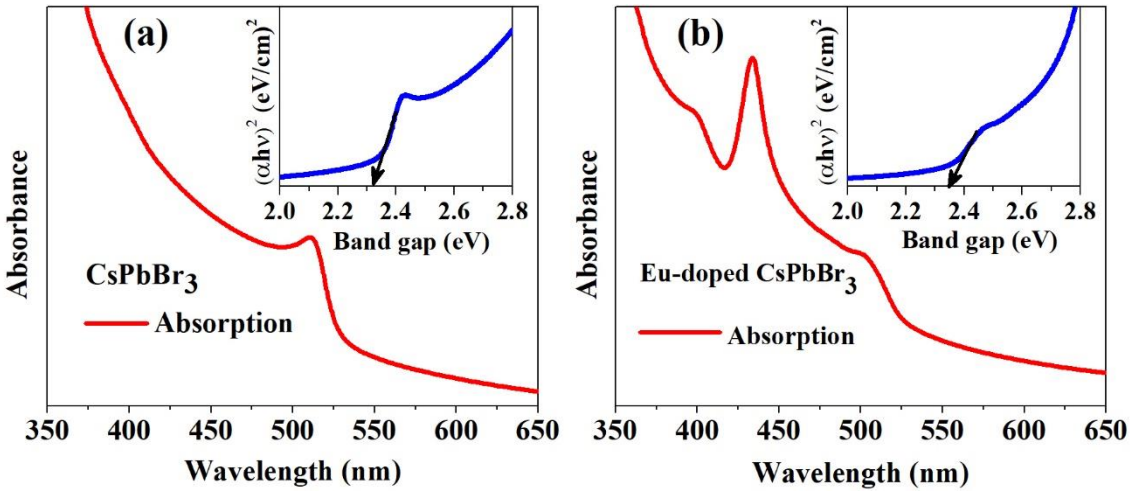

Figure 3.4: UV-visible absorption spectra of (a) $CsPbBr_3$ NCs, and (b) Eu-doped $CsPbBr_3$ NCs. Corresponding insets show the band gaps of $CsPbBr_3$ NCs and Eu-doped $CsPbBr_3$ NCs.

The $CsPbBr_3$ NCs exhibit a distinct absorption peak at 510 nm, which corresponds to the band-to-band transition within $CsPbBr_3$. In contrast, the Eu-doped $CsPbBr_3$ NCs show absorption peaks at 398, 434, and 500 nm. The peaks at 398 nm and 434 nm are attributed to the transitions from the ground state to various excited states, specifically the $4f^7 \rightarrow 4f^6(^7F_J)5d$ transitions of the Eu^{2+}-ion [140]. The absorption band at 398 nm is associated with the electronic, electric dipole transition from $^7F_0 \rightarrow ^5L_6$, while the peak at 434 nm corresponds

to the electric dipole transition $^7F_1 \rightarrow {}^5D_3$. The absorption peak at 500 nm is due to the band-to-band transition of $CsPbBr_3$. These well-defined absorption features in the UV-visible region suggest that this material holds potential for applications in UV and visible light-induced luminescent technologies, including anti-counterfeiting, energy harvesting, light-emitting diodes, and solar cells.

The bandgap of $CsPbBr_3$ and Eu-doped $CsPbBr_3$ NCs is determined using the Wood and Tauc method.

$$\alpha hv = A(hv - E_g)^n \quad \ldots (3.1)$$

Here, α represents the absorption coefficient, hv is the photon energy, E_g represent the bandgap, and n corresponds to the nature of the electronic transitions. The E_g is obtained by extrapolating the linear region of the $(\alpha hv)^n$ versus hv, with the X-intercept of the extrapolated line E_g value. The Tauc plots for both undoped and Eu-doped $CsPbBr_3$ NCs are shown in the insets of Fig. 3.4(a) and 3.4(b), respectively. The measured E_g for $CsPbBr_3$ NCs is 2.31 eV, consistent with previously reported values [141]. Upon doping $CsPbBr_3$ with Eu ions, the bandgap increases slightly to 2.35 eV. This small increase in bandgap is likely due to a reduction in particle size of Eu-doped $CsPbBr_3$ compared to $CsPbBr_3$ as observed in HR-TEM analysis.

3.3.3 Fourier transform infrared (FT-IR) study

FT-IR analysis was conducted to investigate the vibrational modes of functional groups in the synthesized samples using the Nicolet iS5, Thermofisher, within the 400–4000 cm^{-1} range. Fig. 3.5(a) and 3.5(b) display the FT-IR spectra of $CsPbBr_3$ and Eu-doped $CsPbBr_3$

NCs, respectively. Table 3.2 lists the vibrational energies corresponding to the various functional groups present in the samples.

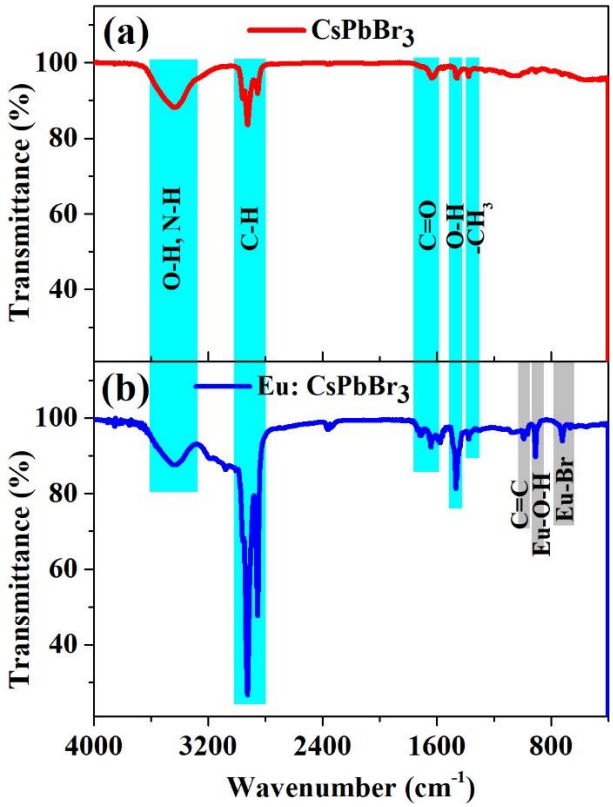

Figure 3.5: FTIR spectra of (a) $CsPbBr_3$, and (b) Eu-doped $CsPbBr_3$ NCs.

The peak observed at 3433 cm^{-1} corresponds to the stretching vibration of the N-H group, which is also influenced by the O-H stretching vibration from the –OH functional group [142][143]. The asymmetric and symmetric vibrations of the C-H bonds in the long alkyl chains of organic ligands OA and OAm are seen at 2924 cm^{-1} and 2853 cm^{-1}, respectively [144]. Additionally, peaks at 2924 cm^{-1}, 2853 cm^{-1}, and 2955 cm^{-1} may be attributed to alkene groups CH, CH_2, and CH_3 [145]. The carbonyl group, identified by C=O stretching, shows a peak at 1712 cm^{-1} and another contribution at 1641 cm^{-1}, while the C=C bond exhibits a vibrational peak at 1577 cm^{-1} and additional peaks in the 900–1000 cm^{-1} range [145][146]. The 1641 cm^{-1} peak is also associated with the bending vibration mode of

adsorbed water on the sample's surface. Carboxylic O-H bending is indicated by a peak at 1466 cm^{-1} [147]. The peak at 1377 cm^{-1} corresponds to the $–CH_3$ group, and the C-O-C stretching vibration is found at 1075 cm^{-1} [143]. The peaks at 996 cm^{-1} and 992 cm^{-1} are indicative of the metal-oxygen (Eu-O) bond, while the Eu-O-H bond is represented by a peak at 909 cm^{-1} [148]. The characteristic peak at 721 cm^{-1} is due to the Eu–Br bond [145]. These 996, 992, 909, and 721 cm^{-1} peaks are absent in the FT-IR spectrum of $CsPbBr_3$ but present in the Eu-doped $CsPbBr_3$ spectrum, confirming the incorporation of Eu into the lattice structure.

Table 3.2 Different vibrational modes observed in the FTIR spectra of $CsPbBr_3$, and (b) Eu-doped $CsPbBr_3$ NCs.

Vibrational Energy (cm^{-1})	**Vibrational modes**
3433	N–H, O–H stretching vibration
2924	C–H, asymmetric vibration
2853	C–H, symmetric vibration
1712, 1641	C=O, stretching vibration
1577, 996, 992	C=C bond
1466	O–H bending vibration
1377	-CH_3 functional group
1075	C–O–C stretching vibration
909	Eu-O-H vibration
721	Eu-Br vibration

3.3.4 X-ray photoelectron spectroscopy (XPS) analysis

To determine the valence states of various elements in Eu-doped $CsPbBr_3$, X-ray photoelectron spectroscopy (XPS) was performed using a Thermo Fisher Scientific K-Alpha system, covering an energy range of 0-1350 eV. The survey spectrum of Eu-doped $CsPbBr_3$is

shown in Fig. 3.6(a). The high resolution XPS spectra for Cs, Pb, Br, and Eu are presented in Fig. 3.6(b), 3.6(c), 3.6(d), and 3.6(e), respectively. For Cs, the binding energies for the $3d_{3/2}$ and $3d_{5/2}$ core levels are observed at 737.68 eV and 723.68 eV, respectively [149]. The Fig. 3.6(c) depict the Pb binding energies of 142.58 eV and 137.68 eV for the $4f_{5/2}$ and $4f_{7/2}$ levels. The Br is characterized by binding energies of 68.67 eV and 67.60 eV for the $3d_{3/2}$ and $3d_{5/2}$ levels, respectively.

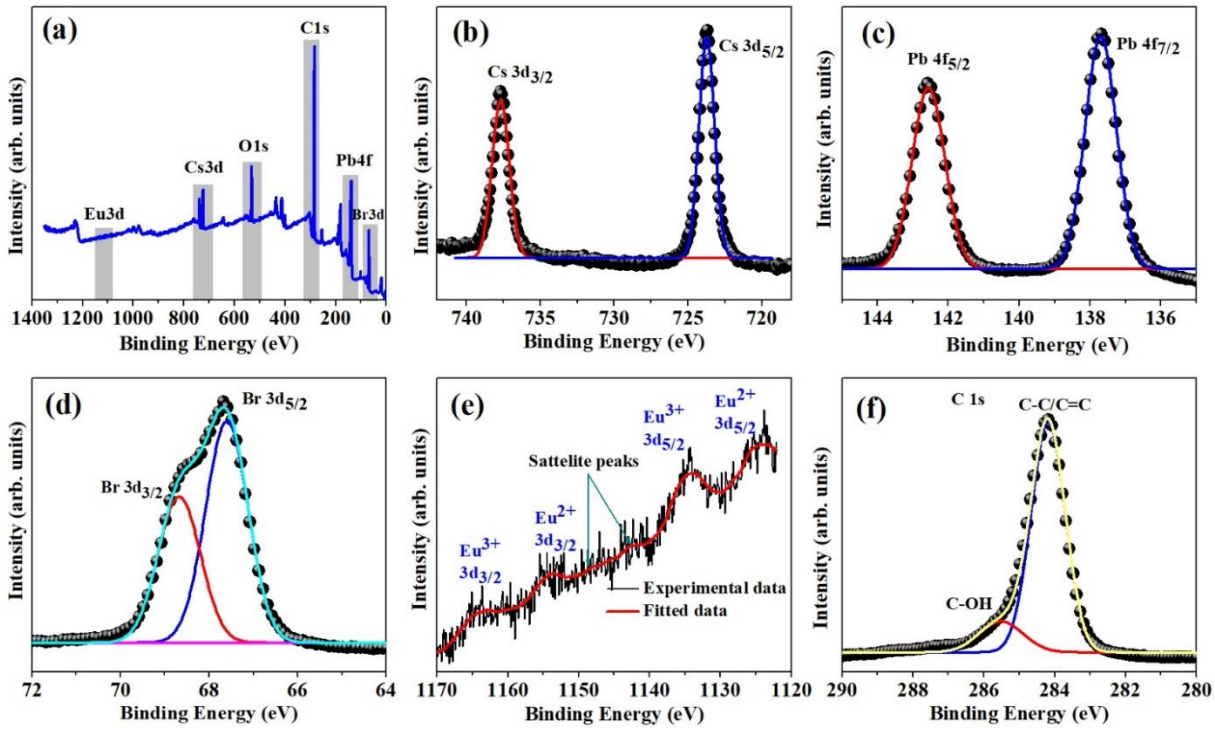

Figure 3.6: (a) XPS survey spectrum of Eu-doped $CsPbBr_3$ NCs. High-resolution XPS spectra of (b) Cs3d, (c) Pb4f, (d) Br3d, (e) Eu3d, and (f) C1s orbitals.

The Eu-3d core level spectrum reveals four peaks at approximately 1164.6 eV, 1153.9 eV, 1134.2 eV, and 1124.1 eV. The peaks at 1124.1 eV and 1134.2 eV correspond to the $3d_{5/2}$ core level of Eu^{2+} and Eu^{3+}, respectively, while the peaks at 1153.9 eV and 1164.6 eV are associated with the $3d_{3/2}$ core level of Eu^{2+} and Eu^{3+}, respectively [150]. These peak indicate the presence of both 2+ and 3+ oxidation states of Eu in the sample. The observed small satellite peaks result from chemical shifts between Eu^{2+} and Eu^{3+} states. The reduction

of Eu^{3+} to Eu^{2+} can be attributed to two main factors [151]: (1) the substitution of trivalent Eu^{3+}-ions for divalent Pb^{2+} ions and (2) the similar ionic radii of Eu^{2+} and Pb^{2+}-ions. Consequently, when Eu^{3+}-ion replace Pb^{2+}, charge neutrality is maintained by requiring two Eu^{3+}-ions for every three Pb^{2+}-ions.

Upon doping, each Eu^{3+}-ion into the $CsPbBr_3$ host lattice, a negatively charged vacancy defect, V_{Pb}, and two positively charged Eu_{Pb} defects are generated [151]. The V_{Pb} acts as an electron donor, while Eu_{Pb} as an electron acceptor. Under certain stimulation methods, such as thermal energy or photon exposure, the negative charge from V_{Pb} may migrate to the Eu^{3+} site within the lattice, reducing Eu^{3+} to Eu^{2+}. Since XPS is a surface-sensitive technique with a depth of up to 10 nm, some Eu^{2+} ions on the surface are exposed to air post-synthesis and undergo oxidation to Eu^{3+} [152]. As a result, both +2 and +3 oxidation states of Eu are observed in the XPS spectrum. However, no emission is detected from Eu^{3+} in emission spectrum, suggesting that it is predominantly present on the surface, while Eu^{2+} occupies the Pb^{2+} lattice sites within the host, contributing to the characteristic emission. The XPS survey scan also reveals the presence of the O1s peak, attributable to the OA and OAm used in synthesis [139]. The C1s peak in the XPS spectrum is due to the various organic solvents used during synthesis, with a binding energy of 284.18 eV. The characteristic peaks of each constituent element in the XPS spectra confirm the presence of all components in the synthesized NCs.

3.3.5 Photoluminescence (PL) study

The photoluminescence (PL) excitation and emission spectra measurement were conducted using a Horiba Fluorolog-3 spectrophotometer, where a 450 W Xenon lamp served as the excitation source and a photomultiplier tube (PMT) functioned as the detector.

PL analysis is an effective method to confirm the presence of Eu^{2+}-ions in the samples [151]. The excitation spectra for both $CsPbBr_3$ and Eu^{2+}-doped $CsPbBr_3$ NCs are presented in Fig. 3.7(a) and 3.7(c), respectively, and are consistent with previously reported data [153]. In both cases, the excitation spectra are broad, likely due to band-to-band transitions from the valence band to the conduction band of $CsPbBr_3$. Such broadband excitation is also observed in Eu^{2+}-activated $LiSr_4(BO_3)_3$ [154]. Additionally, in the Eu^{2+}-doped $CsPbBr_3$, distinct small peaks are observable. The Eu^{2+} ions exhibit parity-allowed $4f^7$-$4f^6$5d transitions, resulting in a broad excitation band [155]. This transition is an electric-dipole-allowed process, where Eu^{2+} transitions from the ground state $^8S_{7/2}4f^7$ to the excited state $4f^65d^1$. The f-d excitation transition of Eu^{2+}-ion is complex due to several factors: in the $4f^65d^1$ excited state, the 5d electron is influenced by crystal field splitting [156]. Additionally, spin-orbit coupling causes the $4f^65d^1$ excited state of Eu^{2+} to split into ^7F_J (J = 0–6) multiplets, broadening the band into a non-Gaussian "staircase" structure. Moreover, the interaction between the 5d electron and the core $4f^6$ electrons of the Eu^{2+}-ion results in overlapping excitation bands. The emission spectra of $CsPbBr_3$ and Eu^{2+}-doped $CsPbBr_3$ NCs are depicted in Fig. 3.7(b) and 3.7(d), respectively. The $CsPbBr_3$ NCs display a sharp emission peak in the green region, centered at 515 nm with a full width at half maximum (FWHM) of 24 nm when excited at 406 nm [139]. This sharp emission is indicative of band-edge emission in $CsPbBr_3$ NCs. The Eu^{2+}-doped $CsPbBr_3$ NCs) exhibit two distinct emission peaks when excited at the same wavelength as the $CsPbBr_3$. These peaks occur at 498 nm in the green region and 442 nm in the blue region [157]. The FWHM of the green and blue emissions are 20 nm and 13 nm, respectively. The sharp blue emission at 442 nm originates from the $4f^6(^7F_J)5d^1 \rightarrow 4f^7$ transition of Eu^{2+}-ion

[140]. The green emission at 498 nm is attributed to a blue-shifted band-edge emission of $CsPbBr_3$ [153].

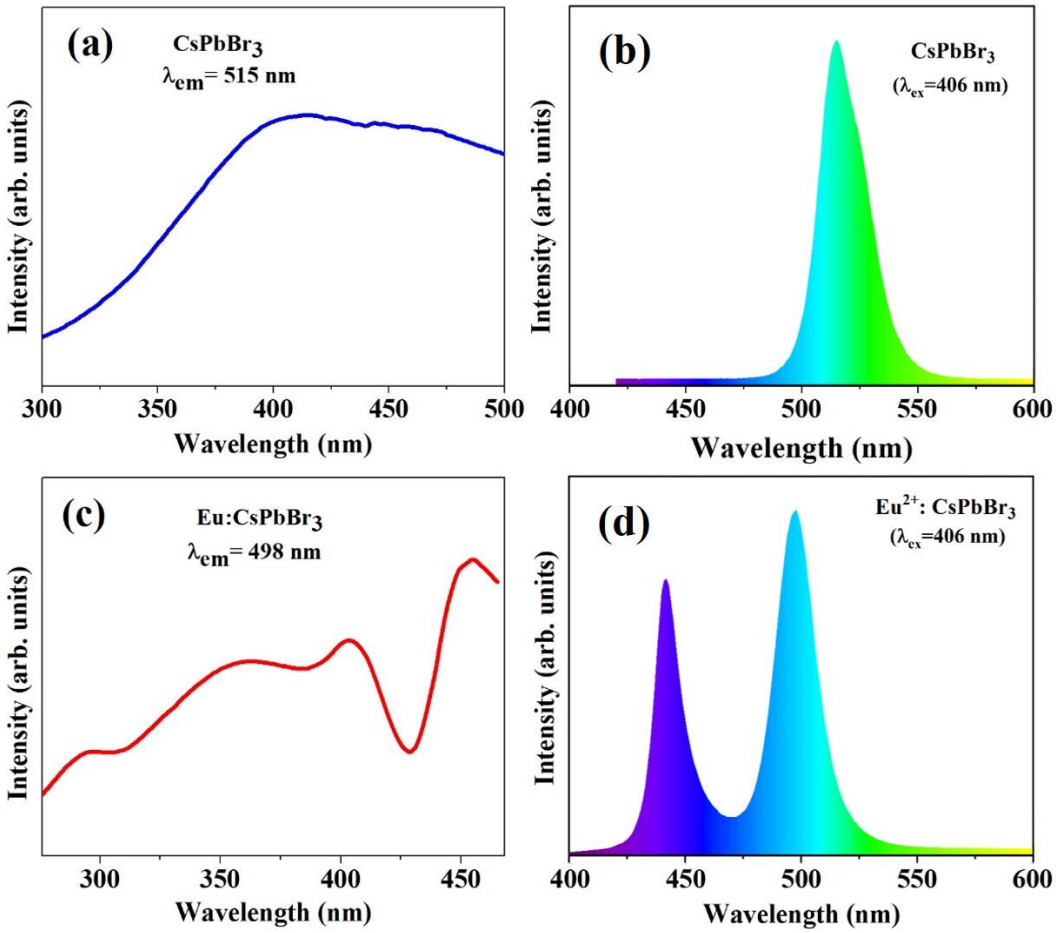

Figure 3.7: (a) Excitation (λ_{em} = 515 nm), and (b) emission (λ_{ex} = 406 nm) spectra of $CsPbBr_3$ NCs. (c) Excitation (λ_{em} = 498 nm), and (d) emission (λ_{ex} = 406 nm) spectra of Eu: $CsPbBr_3$ NCs**.**

The emission peak associated with Eu^{3+}-ion is not observed in the emission spectrum, indicating that Eu^{2+}-ions are effectively integrated into the crystal lattice at Pb^{2+} sites. While Eu^{3+}-ions remain segregated on the surface and do not contribute to the emission [152]. The PL study of Eu-doped $CsPbBr_3$ reveals that the energy transfer from $CsPbBr_3$ to Eu^{2+} ions, as illustrated in Fig. 3.8(c). The emission band of Eu^{2+} is influenced by the surrounding ions at its occupied site [155]. The Eu^{2+} orbital is sensitive to the local crystal field, the radiative

relaxation of Eu^{2+}-ion varies slightly with the host matrix, as observed in the emission spectra. Emission transitions from Eu^{2+}-ions in different hosts are summarized in Table 3.3.

Table 3.3 The emission peak wavelength of the Eu^{2+}-ion doped in different hosts.

Hosts matrix	**Excitation (nm)**	**Emission (nm)**	**Reference**
$LiSr_4(BO_3)_3$	400	630	[154]
$SrAl_{12}O_{19}$	275	397	[158]
$SrAl_4O_7$	290	470	[158]
$Sr_4Al_{14}O_{25}$	290	490	[158]
$SrAl_2O_4$	350	520	[158]
$Sr_3Al_2O_6$	467	625	[158]
$Li:PoO_4$	340	594, 615	[159]
$Rb_3YSi_2O_7$	450	622	[130]
$CaMgSi_2O_6$	356	451	[156]
$KbaPO_4$	350	430	[160]
$CaSiO_3$	450	618	[161]
$SrSiO_3$	420	550	[161]
$SrCaP_2O_7$	330	450	[131]
$CsPbBr_3/CaAl_2O_4$	330	440	[157]
$CsPbBr_3$	365	440	[152]
$CsPbBr_3$	406	442	This work

The synthesized Eu^{2+}: $CsPbBr_3$ NCs exhibit broad excitation across the 250-475 nm range, similar to the excitation band observed in Eu^{2+}-activated $LiSr_4(BO_3)_3$ [154]. The emission peak of Eu^{2+} varies across different host lattices, as listed in Table 3.3 as also summarized by Lyu et al. [129]. The peak position variation is likely due to the strong influence of the atomic environment surrounding the Eu^{2+}-ion within the lattice. Digital photographs of $CsPbBr_3$ NCs and Eu-doped $CsPbBr_3$ NCs dispersed in toluene under daylight and UV light

are shown in Fig. 3.8(d). The different color appearances under varying light conditions suggest the potential of this material for anti-counterfeiting application.

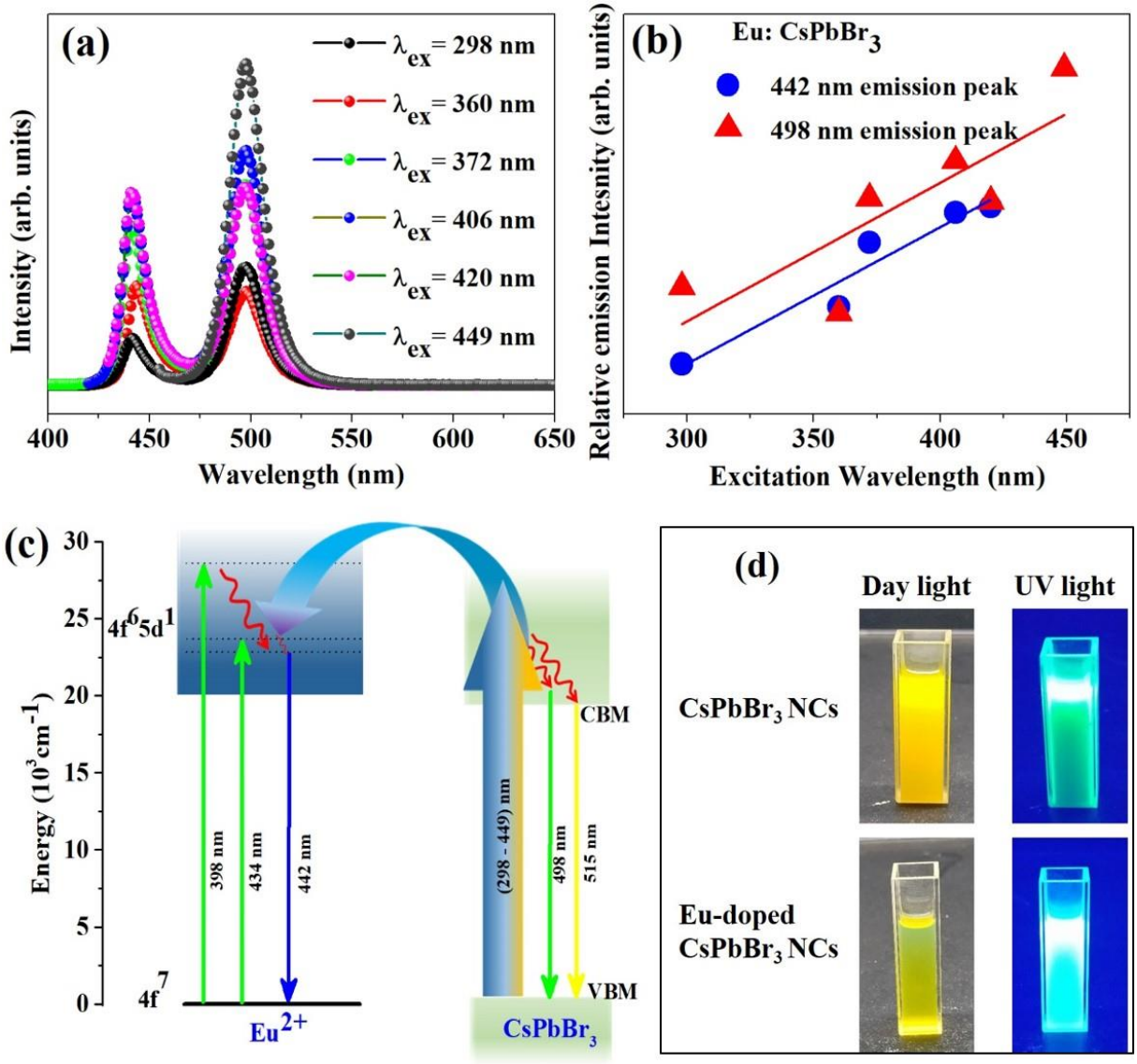

Figure 3.8: (a) The PL spectra of Eu^{2+}-doped $CsPbBr_3$ NCs for different excitation wavelength. (b) Excitation wavelengths dependent emission peak intensity variation of Eu^{2+}-doped $CsPbBr_3$ NCs. (c) Partial energy level diagram along with a schematic representation of the energy transfer from $CsPbBr_3$ to Eu^{2+}-ion. (d) Digital photographs of $CsPbBr_3$ and Eu-doped $CsPbBr_3$ NCs (dispersed in toluene) under UV and daylight.

To investigate the variation in luminescence intensity caused by electric and magnetic dipole transitions in Eu^{2+}-doped $CsPbBr_3$ NCs, the PL spectra were recorded at various excitation wavelengths, including 298, 360, 372, 406, 420, and 449 nm. The luminescence

intensity was found to depend on the excitation wavelength illustrated in Fig. 3.8(b). A linear fit of the peak intensity at 442 nm indicates that the peak intensity increases with increasing excitation wavelength. The blue band emission also follows this trend, with two anomalies at 360 nm and 420 nm excitations. At these wavelengths, the emission intensities of the bands at 442 nm and 498 nm are nearly equal. Due to the presence of prominent absorption band between 410-448 nm associated with the Eu^{2+}-ion, the excitation photons are captured equally by both the Eu^{2+} ion and the $CsPbBr_3$ host. This results approximately the same emission intensity for both the 442 nm and 498 nm peaks. A similar effect is observed at the 360 nm excitation. However, further study is needed to fully understand the reasons behind this behavior. The different emission intensities observed at different excitation wavelengths could be attributed to several factors: (1) the overlap of interaction parameters between the ground and excited states, (2) exchange interactions among the various types of atoms or ions present in the system, and (3) the density of incoming photons on the sample etc. [159].

3.3.6 Time-resolved photoluminescence (TRPL) study

The time-resolved photoluminescence (TRPL) investigation was conducted to analyze the carrier dynamics within $CsPbBr_3$ and Eu^{2+}-doped $CsPbBr_3$ NCs, utilizing an FLS980 Edinburgh spectrometer equipped with a pulsed diode for excitation. The PL decay times were examined under 266 nm pulsed excitation. Fig. 3.9 presents the resulting decay curves for both $CsPbBr_3$ and Eu^{2+}-doped $CsPbBr_3$ NCs. The decay curve and its corresponding exponential fit for the $CsPbBr_3$ NCs are illustrated in Fig. 3.9(a). The decay data were fitted using an exponential function as described by the following equation:

$$I(t) = B_0 + \sum_i A_i \exp\left(-\frac{t}{\tau_i}\right) \quad \ldots (3.2)$$

In bi-exponential fitting, the time constant τ_1 represents the fast decay process associated with trap-assisted non-radiative recombination, while τ_2 corresponds to the slower decay process, which is attributed to the radiative recombination of free charge carriers. The parameter B_0 is a constant, and A_i denotes the decay amplitude associated with each decay time τ_i. The $CsPbBr_3$ NCs exhibit bi-exponential decay, with τ_1 and τ_2 values of 0.68 ns and 10.97 ns, respectively. Upon doping $CsPbBr_3$ with Eu^{2+}-ion, two distinct emission peaks appear at 442 nm and 498 nm. The TRPL decay for both emission peaks were recorded using the same excitation wavelength of 266 nm. The decay and their corresponding fitted curves are depicted in Fig. 3.9(b) and 3.9(c) for the emission peaks at 498 nm and 442 nm, respectively. The decay curve of the 498 nm emission wavelength displays a single-exponential behavior. Whereas the decay curve for 442 nm exhibits a bi-exponential nature, with τ_1 and τ_2 values of 3.86 ns and 15.59 ns, respectively. For bi-exponential decay curves, the average decay time is calculated using the formula

$$\tau_{av} = \frac{A_1\tau_1^2 + A_2\tau_2^2}{A_1\tau_1 + A_2\tau_2} \quad \ldots (3.3)$$

The symbols, as defined earlier, hold their respective meanings. Table 3.4 lists the individual decay times obtained from data fitting and the calculated average decay times (τ_{av}) using equation (3.3) for $CsPbBr_3$ NCs and Eu^{2+}-doped $CsPbBr_3$ NCs. The calculated τ_{av} for $CsPbBr_3$ NCs, derived from the parameters of a bi-exponential fit, is 7.27 ns. In $CsPbBr_3$, excitons are rapidly captured by bromide-vacancy defects, as reflected in the decay curve in Fig. 3.9(a). For Eu^{2+}-doped $CsPbBr_3$ NCs, the average decay time for the 498 nm emission is 5.80 ns, while for the 442 nm emission, it is 8.89 ns. A noticeable reduction in the τ_{av} of the host emission (498 nm) is observed in the Eu^{2+}-doped $CsPbBr_3$ NCs compared to the

undoped $CsPbBr_3$ NCs. This reduction may be attributed to energy transfer from $CsPbBr_3$ to the Eu^{2+}-ions.

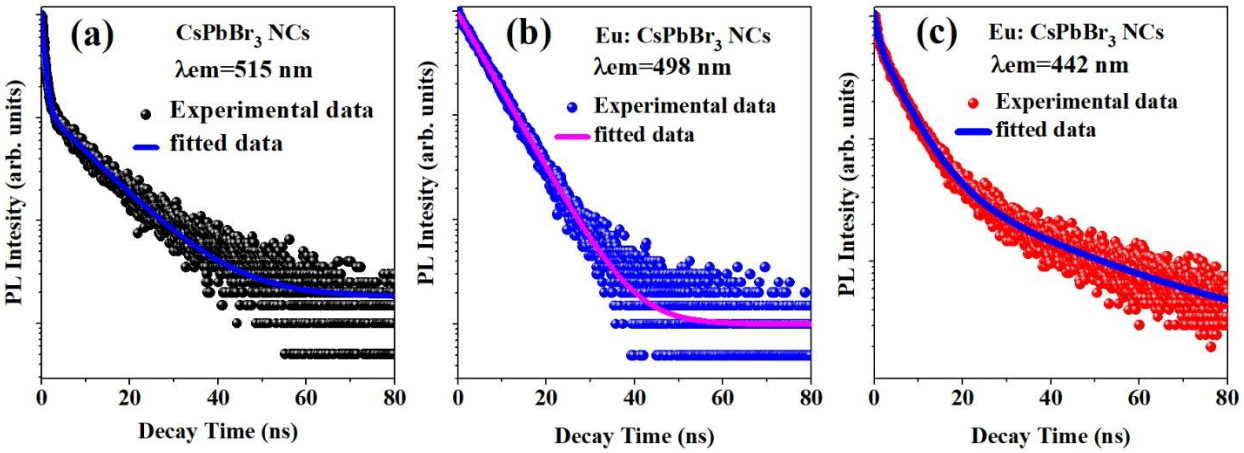

Figure 3.9: TRPL decay curves of the (a) $CsPbBr_3$ NCs emission monitored at 515 nm. Eu-doped $CsPbBr_3$ NCs emission monitored at (b) 498 nm, and (c) 442 nm**.**

Also, in $CsPbBr_3$, the bromide vacancies formation is quite common, and these defects act as luminescence quenchers [162]. These bromide-vacancy defects quickly capture the excitons, which reduces the band-edge exciton density and enhances non-radiative recombination pathways. Doping Eu^{2+} in $CsPbBr_3$ mitigates the formation of bromide vacancies, leading to a significant improvement in the radiative recombination channel. This is evidenced by the increased PL decay time as observed in Eu^{2+}-doped $CsPbBr_3$ NCs.

Table 3.4 TRPL decay parameters of the $CsPbBr_3$ and Eu-doped $CsPbBr_3$ NCs.

Sample	$\lambda_{ex}\lambda_{em}$ **(nm)**	**B_0**	**B_1**	τ_1**(ns)**	**B_2**	τ_2**(ns)**	χ^2	τ_{avg} **(ns)**
$CsPbBr_3$	266/515	1.70	2105.51	0.68	232.42	10.97	1.20	7.27
Eu^{2+}:$CsPbBr_3$	266/498	1.16	1908.04	5.86	-	-	1.03	5.80
	266/442	7.38	1431.78	3.86	266.45	15.59	1.65	8.89

The decay time of Eu^{2+} emission varies depending on the host matrix [163]. For instance, the τ_{av} of Eu^{2+} emission in $K_2SrP_2O_7$ host is reported to be 140 ns [133], while in CsBr, it is 342 ns [163]. Additionally, the decay time of Eu^{2+} emission has been reported in the microsecond

(μs) range. The τ_{av} values of 3.0 μs in $BaSi_2O_5$ [129] and 1.15 μs in $KCaCl_3$ also reported [134]. The variation in the decay times of Eu^{2+} emission is likely due to the influence of the surrounding atomic environment at the Eu^{2+}-ion site [129]. These characteristics of Eu^{2+}-ions make them promising candidates for various sensing and probing applications.

3.3.7 Commission International de I′ Eclairage (CIE) chromaticity study

The CIE chromaticity diagram is a crucial analytical tool to study the assess the overall color of the emission spectrum of the sample, particularly in terms of how they are perceived by the human eye. This diagram is especially important when examining materials intended for lighting applications, such as display devices color and color or white light-emitting diodes (LEDs).

The CIE 1931 (x, y) coordinate plot of the emission spectra for the synthesized $CsPbBr_3$ and Eu^{2+}-doped $CsPbBr_3$ is presented in Fig. 3.10. The CIE (x, y) coordinate of $CsPbBr_3$ emission is (0.0988, 0.7645), placing it in the green region. In contrast, the Eu^{2+}-doped $CsPbBr_3$ exhibits CIE (x, y) coordinates in the blue region. The CIE coordinates of Eu^{2+}-doped $CsPbBr_3$ under various excitation wavelengths are calculated and listed in Table 3.5. Notably, there is minimal deviation in the CIE coordinates under different excitation wavelengths, as shown in Fig. 3.10. The zoomed-in view of CIE diagram for the excitation wavelengths of 372 nm and 406 nm is depicted in Fig. 3.10(b), whereas for the 260 nm and 420 nm excitation shown in Fig. 3.10(c). Furthermore, the luminous efficacy of optical radiation (LER), which quantifies how efficiently light is perceived by the human eye, was calculated using the software "Color Calculator v7.7" for both the $CsPbBr_3$ and Eu-doped $CsPbBr_3$ samples. The LER for $CsPbBr_3$ emission is 447 lm/W, whereas for the Eu-doped $CsPbBr_3$, it ranges between 138-179 lm/W.

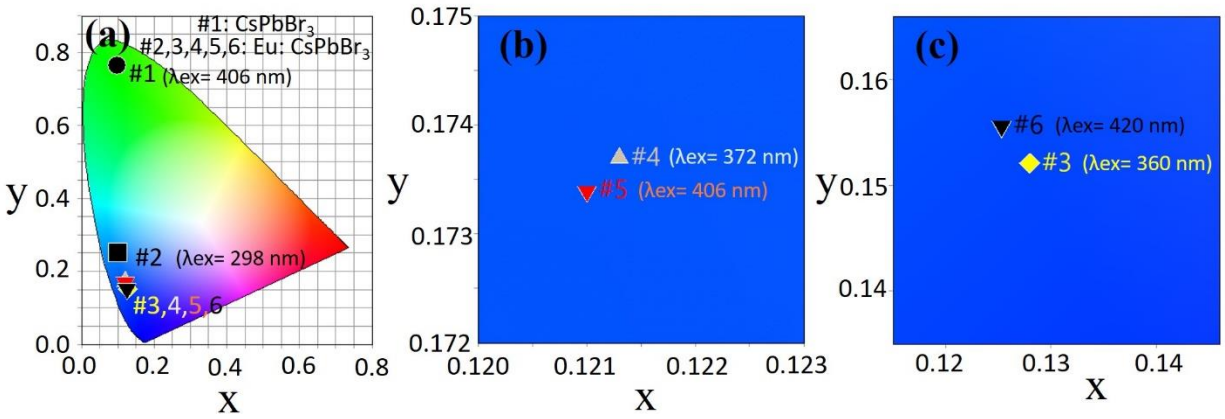

Figure 3.10: CIE chromaticity diagram of the (a) $CsPbBr_3$ and Eu-doped $CsPbBr_3$ NCs. Integrated CIE chromaticity diagram of Eu-doped $CsPbBr_3$ NCs for the excitation wavelengths (b) (372 nm, and 406 nm), and (c) (260 nm, and 420 nm).

Table 3.5 CIE parameters of the $CsPbBr_3$ and Eu-doped $CsPbBr_3$ NCs PL emission.

Composition	**λ_{ex} (nm)**	**CIE (x, y) coordinate**	**LER (lm/W)**	***CP* (%)**
$CsPbBr_3$	406	0.0988, 0.7645	447	86.7
Eu:$CsPbBr_3$	298	0.1004, 0.2509	178	85.0
Eu:$CsPbBr_3$	360	0.1280, 0.1521	138	86.1
Eu:$CsPbBr_3$	372	0.1213, 0.1737	147	85.8
Eu:$CsPbBr_3$	406	0.1210, 0.1734	148	85.9
Eu:$CsPbBr_3$	420	0.1253, 0.1557	139	86.6

Color purity (*CP*) is an another crucial parameter in lighting applications. It represents the weighted average of the CIE color coordinates (x, y) of the emitted light from the sample relative to those of the CIE illuminant and the dominant wavelength (λ_d) coordinates [164]. The λ_d corresponds to the wavelength that appears as the monochromatic wavelength in the light source's spectrum. The *CP* of the $CsPbBr_3$ and Eu-doped $CsPbBr_3$ emission spectra is calculated using the following equation:

$$CP = \sqrt{\frac{(x - x_i)^2 + (y - y_i)^2}{(x_d - x_i)^2 + (y_d - y_i)^2}} \times 100 \qquad \ldots (3.4)$$

In this equation, (x, y) represents the CIE color coordinates of the emitted light from the sample, while (x_i, y_i) represents the CIE illuminant coordinates, given as (0.3101, 0.3162). The CIE coordinate of the λ_d is denoted as (x_d, y_d). This coordinate is determined by drawing a straight line from the CIE illuminant through the emitted light's (x, y) coordinates on the CIE diagram. The point where this line intersects the perimeter of the CIE diagram provides the coordinate of λ_d. The *CP* of the synthesized sample exceeds 85% under various excitation wavelengths, as listed in Table 3.5. This high *CP* value indicates that the sample is potentially efficient for colored lighting applications. The results, derived from the CIE 1931 color study, suggest that this material has promising potential for use in display technologies and color LEDs.

3.4 Conclusions

In summary, in this Chapter, the structural and optical characteristics of pristine $CsPbBr_3$ and Eu^{2+}-doped $CsPbBr_3$ NCs have investigated. Both the samples were synthesized via hot-injection technique. The pristine $CsPbBr_3$ NCs have an average particle size of 19 nm, which is significantly reduced to approximately 7 nm in the Eu^{2+}-doped $CsPbBr_3$ NCs due to surface modification. The $CsPbBr_3$ NCs exhibit a sharp green emission at 515 nm with a FWHM of about 24 nm. In contrast, the Eu^{2+}-doped $CsPbBr_3$ NCs show two distinct emission peaks at 498 nm with FWHM ~20 nm and 442 nm with FWHM ~13 nm. The additional peak at 442 nm is attributed to the $4f^6(^7F_J)5d^1 \rightarrow 4f^7$ transition of Eu^{2+}-ions. The observed shift in the green emission for the Eu^{2+}-doped $CsPbBr_3$ is attributed to the reduction in average particle size. The E_g for $CsPbBr_3$ NCs is determined to be 2.31 eV, while the E_g increases to 2.35 eV for Eu^{2+}-doped $CsPbBr_3$. Detailed decay dynamics were examined, with the average decay time for the $CsPbBr_3$ emission at 515 nm being 7.27 ns. For the Eu^{2+}-

doped $CsPbBr_3$, the average decay times are 5.80 ns and 8.89 ns for the emission peak 498 nm and 442 nm, respectively. The CIE coordinates of the Eu-doped $CsPbBr_3$ emission spectra were plotted for various excitation wavelengths, showing minimal change. The LER was calculated to be 447 lm/W for $CsPbBr_3$ NCs, while for Eu^{2+}-doped $CsPbBr_3$ NCs, it ranged between 138-179 lm/W. Notably, the color purity of the emission spectra of both the samples under different excitations exceeds 85%. These optical properties suggest that Eu^{2+}-doped $CsPbBr_3$ NCs hold promise as potential candidates for applications in color displays, blue LEDs, and anti-counterfeiting technologies.